RSC Advances

PAPER

View Article Online
View Journal | View Issue

Cite this: *RSC Adv.*, 2026, **16**, 4535

Defect-engineered N-doped carbon stabilizes Cu^+ active sites for bifunctional CO_2 electroreduction to CO and formate

Pirapath Arkasalerks,[a] Phongphot Sakulaue,[ab] Pongkarn Chakthranont,[c] Kanokwan Kongpatpanich[d] and Khanin Nueangnoraj*[a]

The development of bifunctional electrocatalysts capable of steering CO_2 reduction toward selective C_1 products under mild conditions remains central to advancing next-generation electrochemical technologies. Here, we demonstrate that stabilization of Cu^+ species by N-doped carbon derived from tea leaves (TL9) enables highly selective and durable CO_2 electroreduction to CO and formate. Uniformly dispersed Cu_2O nanoparticles supported on TL9 exhibit strong metal–support interactions and form stable Cu–N_x coordination that preserves the active Cu^+/Cu^0 interface during operation. Structural, spectroscopic, and electrochemical analyses reveal that this tailored interface suppresses Cu agglomeration and hydrogen evolution, promoting efficient two-electron transfer pathways. The optimized TL9/Cu-40% catalyst achieves faradaic efficiencies approaching 90% for CO and formate at −0.6 V *vs.* RHE and maintains over 60% selectivity after 24 h of continuous operation. These findings highlight how defect-engineered carbon supports can precisely regulate Cu oxidation states to enhance efficiency, selectivity, and stability—offering a robust design principle for bifunctional catalysts that couple renewable electricity with CO_2 valorization.

Received 20th November 2025
Accepted 6th January 2026

DOI: 10.1039/d5ra08966b

rsc.li/rsc-advances

1. Introduction

The electrochemical reduction of carbon dioxide (CO_2RR) has attracted increasing attention as a viable approach to closing the carbon cycle while generating value-added fuels and chemicals using renewable electricity. Significant progress has been achieved in developing copper-based electrocatalysts, which uniquely enable the formation of a wide spectrum of products ranging from CO and formate to multicarbon (C_2^+) species such as ethylene and ethanol.[1,2] However, achieving high selectivity toward desired products remains a major challenge, as competing hydrogen evolution and complex multi-electron pathways often limit the overall reaction efficiency.[3,4]

Among the various CO_2RR products, CO and formate stand out as particularly attractive due to their simple two-electron transfer pathways. In contrast to C_2^+ products that require high overpotentials, intricate C–C coupling steps, and often suffer from poor durability, the generation of CO and formate is both kinetically and thermodynamically more favorable. Consequently, these reactions can deliver higher faradaic efficiencies (FE) under milder operating conditions, providing a practical route for sustainable CO_2 utilization.[5] Beyond efficiency, these C_1 products serve as versatile intermediates: CO is a cornerstone of syngas chemistry and an essential feedstock for downstream processes such as Fischer–Tropsch and methanol synthesis,[6–8] while formate is a stable liquid fuel that can be used directly in formate fuel cells or upgraded into formic acid and oxalate-derived polymer feedstocks.[5] Formate, in particular, should be regarded not merely as a terminal product but as a key gateway intermediate. Its coupling to oxalate unlocks pathways toward a spectrum of downstream chemicals—including glycolic acid, ethylene glycol, glyoxal, and metal oxalates—offering a more practical and scalable alternative to the direct but less selective C_2^+ formation route. Together, CO and formate represent a complementary product pair, balancing gaseous intermediates for large-scale synthesis with liquid fuels and chemical precursors that integrate seamlessly into existing infrastructures.

The ability of copper to toggle between Cu^+ and Cu^0 oxidation states is widely recognized as a crucial factor governing CO_2RR selectivity. Cu^+ species stabilize key intermediates (*e.g.*, *COOH for CO, *OCHO for formate), whereas Cu^0 facilitates electron transfer and product desorption.[9–11] However, under strongly reducing potentials, Cu^+ tends to convert irreversibly to

[a]*School of Bio-Chemical Engineering and Technology, Sirindhorn International Institute of Technology, Thammasat University, Pathum Thani, 12120, Thailand. E-mail: khanin@siit.tu.ac.th*

[b]*Division of Chemical Engineering, Faculty of Engineering, Rajamangala University of Technology Krungthep, Bangkok 10120, Thailand*

[c]*National Nanotechnology Center (NANOTEC), National Science and Technology Development Agency (NSTDA), Khlong Luang, Pathum Thani, 12120, Thailand*

[d]*Department of Materials Science and Engineering, School of Molecular Science and Engineering, Vidyasirimedhi Institute of Science and Technology, Rayong 21210, Thailand*

metallic Cu.[12] One promising strategy to overcome this limitation is the use of N-doped carbon supports, which can anchor Cu^+ species at defect sites and stabilize them *via* coordination with pyridinic or pyrrolic nitrogen functionalities.[13] By tuning the metal–support interaction and dispersion, such hybrid catalysts can maintain a favorable Cu^+/Cu^0 balance during operation, thereby enhancing both selectivity and stability. Previous studies have demonstrated that N-doped carbon supports play a crucial role in stabilizing Cu-based active sites for selective CO_2 electroreduction. Porous N-doped carbon-supported Cu catalysts have achieved high efficiencies toward C_1 products such as CO and formate by promoting CO_2 adsorption and stabilizing Cu^+ species.[9] Similarly, Cu_2O/Cu-based composites immobilized on N-doped graphene have shown enhanced formate selectivity at low overpotentials through synergistic metal–support interactions that suppress hydrogen evolution and facilitate charge transfer.[14] These reports collectively highlight the importance of nitrogen-containing carbon supports in regulating Cu oxidation states and reaction pathways.

In this study, we systematically investigate Cu_2O nanoparticles supported on N-doped carbon derived from tea leaves and compare their CO_2RR performance with those supported on commercial activated carbon. We demonstrate that nitrogen functionalities not only promote uniform dispersion of Cu_2O but also suppress agglomeration and excessive reduction to metallic Cu, resulting in enhanced activity and long-term durability. The optimized catalyst achieves FE approaching 90% for CO and formate at −0.6 V *vs.* RHE and maintains over 60% selectivity after 24 h of continuous operation. These findings highlight the advantages of targeting CO and formate as practical C_1 products and provide mechanistic insights into how support chemistry governs Cu speciation and overall CO_2RR performance.

2. Experimental

2.1 Synthesis of N-doped carbon support

N-Doped carbon derived from tea leaves was synthesized following a previously reported procedure.[15] Briefly, the precursor was prepared by carbonizing and activating tea leaves pretreated with potassium carbonate (K_2CO_3) at a weight ratio of 1 : 1.5. Activation was conducted in a horizontal tubular furnace at 900 °C with a heating rate of 5 °C min^{-1} and held for 1 hour under a continuous N_2 flow of 200 cm^3 min^{-1}. The resulting material was thoroughly washed with RO water and dried at 105 °C overnight. The sample was denoted as TL9, where "9" refers to the activation temperature of 900 °C.

2.2 Preparation of copper/carbon composites

Solution A was prepared by dissolving 1.11 g of copper(II) acetate monohydrate ($Cu(CH_3COO)_2 \cdot H_2O$) in 25 mL of distilled water and stirring at 70 °C for 10 min. Subsequently, 0.6 g of TL9 was introduced into the solution and sonicated for 10 min to ensure homogeneous dispersion. In parallel, solution B was prepared by dissolving 0.95 g of NaOH and 0.83 g of ascorbic acid in 20 mL of distilled water. Solution B was then added dropwise to solution A under continuous stirring, and the reaction was maintained for 30 min. The resulting product was collected by filtration, thoroughly washed with distilled water, and dried to obtain the TL9/Cu-*x*% composite, where *x* denotes the Cu_2O content in wt%. For comparison, YEC/Cu-40% was synthesized by replacing TL9 with commercial activated carbon (YEC-8A) under otherwise identical conditions.

2.3 Material characterizations

X-ray diffraction (XRD) patterns were obtained using a PANalytical Empyrean diffractometer with Cu Kα radiation (λ = 0.15406 nm) over a 2θ range of 10°–80° at a step size of 0.02°. The morphology and elemental composition were analyzed by scanning electron microscopy equipped with energy-dispersive X-ray spectroscopy (SEM-EDS, HITACHI SU8020). Transmission electron microscopy (TEM, HITACHI HT7700) was employed to examine the particle size and lattice fringes of Cu_2O nanoparticles. N_2 adsorption–desorption isotherms were recorded at −196 °C using a MicrotracBEL BELSORP mini-X analyzer to evaluate the textural properties. All samples were degassed under vacuum (10^{-3} kPa) at 150 °C for 6 hours prior to measurement. The specific surface area (S_{BET}) was calculated by the Brunauer–Emmett–Teller (BET) method. The total pore volume (V_{total}) was estimated from adsorption data at P/P_0 = 0.99, while the micropore volume (V_{micro}) was obtained using the Dubinin–Radushkevich (DR) equation. The mesopore volume (V_{meso}) was determined by subtracting V_{micro} from V_{total}.

X-ray photoelectron spectroscopy (XPS) was performed on a JEOL JPS-9010 MC with a Mg Kα source (12 kV, 25 mA) under a base pressure of 10^{-7} Pa. Thermogravimetric analysis (TGA, Mettler Toledo TGA/DSC 1) was used to quantify the Cu_2O loading in the composites. H_2 temperature-programmed reduction (H_2-TPR, BELCAT-B, BEL Japan Inc.) was conducted to evaluate the reducibility and dispersion of Cu_2O nanoparticles.[16] Approximately 20 mg of sample was reduced *in situ* under a flow of 5% H_2/Ar from room temperature to 800 °C at a heating rate of 5 °C min^{-1}. Raman spectra were acquired using a Horiba LabRAM HR Evolution spectrometer with a 532 nm excitation laser to assess graphitization and defect density. The ratio of disordered (D) to graphitic (G) band intensities (I_D/I_G) was determined from deconvoluted peak intensities.

2.4 Electrochemical measurements

Electrochemical measurements were performed in a two-compartment, gas-tight glass H-cell separated by an anion exchange membrane (AMVN). A Pt plate (1.0 × 1.0 cm^2) and a Hg/HgOH electrode in 1 M NaOH served as the counter and reference electrodes, respectively. The working electrode consisted of the catalyst coated onto carbon paper (Toray, TGP-H-120, 1.0 × 1.0 cm^2).

The catalyst ink was prepared by mixing the catalyst, carbon black, and polyvinylidene fluoride (PVDF) in a weight ratio of 8 : 1 : 1 in *N*-methyl-2-pyrrolidone (NMP) to form a homogeneous slurry. Carbon black was added to enhance electrical

conductivity and facilitate electron transport across the electrode.[17] The ink was applied to the carbon paper using a doctor blade (250 μm thickness) and dried under vacuum at 80 °C overnight. The electrolyte (0.5 M $KHCO_3$) was continuously saturated with CO_2 at a flow rate of 20 sccm, and all experiments were conducted at room temperature.

Electrochemical impedance spectroscopy (EIS) was performed prior to CO_2RR testing to determine the solution resistance (R_s) and charge-transfer resistance (R_{ct}) from Nyquist plots. R_s was used to correct the *iR* drop, and all potentials were converted from the Hg/HgOH reference to the reversible hydrogen electrode (RHE) scale for accurate comparison of catalytic activity.

Gaseous products (CH_4, C_2H_4, and C_2H_6) were quantified using gas chromatography with a flame-ionization detector (GC-FID) equipped with a Porapak Q (60/80) column and He as the carrier gas. H_2 and CO were analyzed using GC with a thermal-conductivity detector (GC-TCD) equipped with a molecular sieve 5A column and He as the carrier gas. Liquid products were analyzed by high-performance liquid chromatography (HPLC) equipped with a refractive-index detector (RID) using 5 mM H_2SO_4 as the mobile phase and a Shodex SH1011 Sugar column as the stationary phase. Moreover, the formation of formate was verified by ^{1}H NMR spectroscopy of the post-reaction electrolyte using Bruker Avance III™ HD 600 MHz, and D_2O as the solvent. All electrochemical measurements and products quantifications were performed at least three times. The reported FE represent the average values, and the error bars correspond to the standard deviation.

3. Results and discussion

3.1 Structural characteristics of the carbon samples and composites

The porous characteristics of all samples are summarized in Table S1. Both TL9 and YEC exhibit comparable BET surface areas (S_{BET}) and total pore volumes. Their N_2 adsorption–desorption isotherms (Fig. 1a) display combined type I and type IV profiles with H4-type hysteresis loops, indicative of predominantly microporous structures containing a small fraction of slit-like mesopores. The slightly more pronounced hysteresis in TL9 suggests a marginally higher mesopore content than in YEC, consistent with the V_{meso} values in Table S1. However, this difference is relatively minor and unlikely to

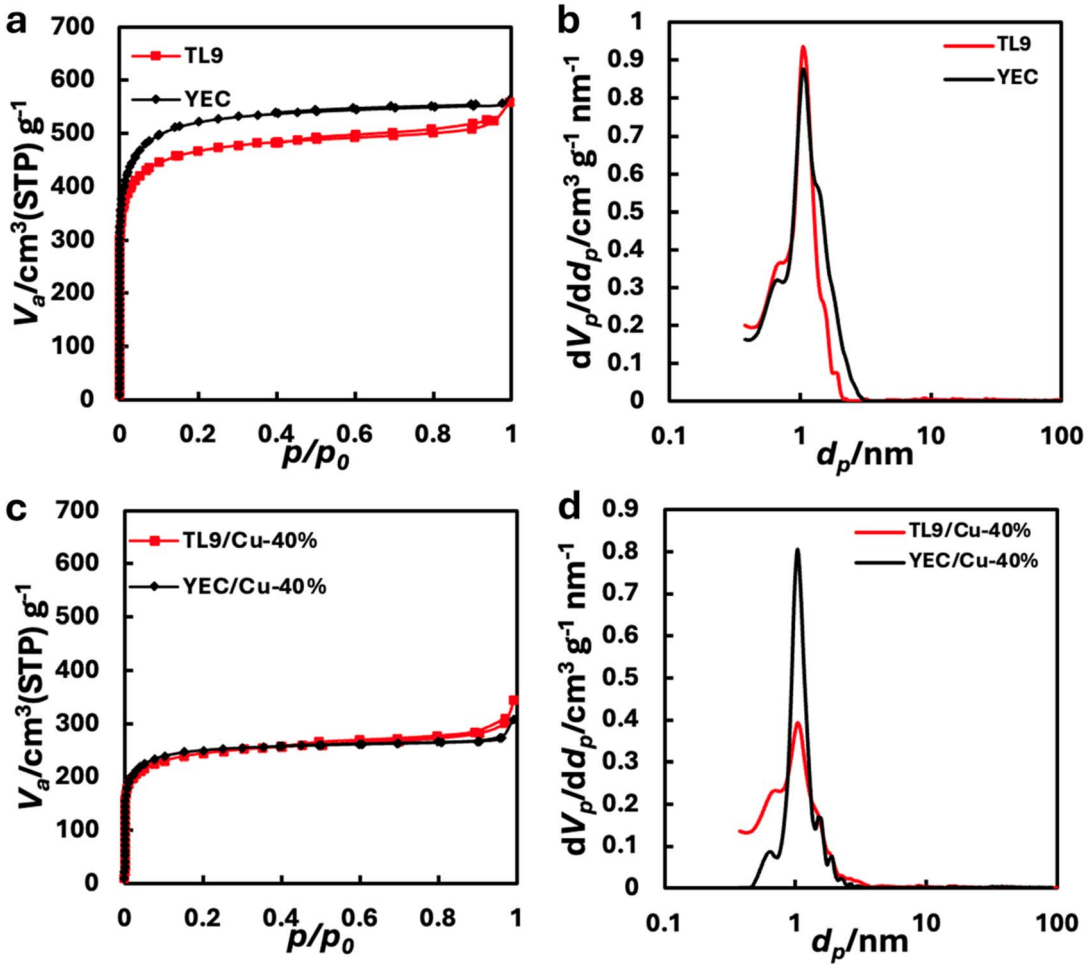

Fig. 1 (a) N_2 adsorption–desorption isotherms and (b) NLDFT pore size distribution of TL9 and YEC samples. (c) N_2 adsorption–desorption isotherms and (d) NLDFT pore size distribution of TL9/Cu-40% and YEC/Cu-40% composites.

significantly affect their comparative electrocatalytic performance. As shown in Fig. 1b, both samples possess similar pore size distributions dominated by micropores (~1 nm).

Upon Cu_2O incorporation, the adsorbed volume and corresponding surface area and pore volume decreased progressively with increasing Cu_2O loading (Fig. S1a). Notably, TL9/Cu-50% exhibits a type II isotherm (Fig. S1b), characteristic of macroporous adsorbents with strong adsorbate–adsorbent interactions,[18] accompanied by a substantial loss of S_{BET} and V_{micro}. This behavior indicates that excessive Cu_2O loading likely blocks or fills the available pores of the carbon support. Fig. 1c compares the isotherms of TL9/Cu-40% and YEC/Cu-40%, both showing combined type I/IV features with H4-type hysteresis loops. The depletion of micropores (~1 nm) observed for TL9/Cu-40% (Fig. 1d) suggests partial blockage of micropores during Cu_2O deposition, whereas the reduction in pore volume of YEC around 1.5 nm implies Cu_2O deposition within larger mesopores or interparticle voids.

Raman spectra of TL9, YEC, TL9/Cu-40%, and YEC/Cu-40% (Fig. 2) exhibit two prominent peaks at ~1340 cm^{-1} (D band) and ~1580 cm^{-1} (G band), corresponding to disordered and graphitic carbon structures, respectively.[19] Deconvolution of the spectra reveals four components: D* (~1200 cm^{-1}), D (~1340 cm^{-1}), D** (~1530 cm^{-1}), and G (~1590 cm^{-1}), representing various C=C stretching and C–H wagging modes associated with structural disorder.[20] The degree of disorder, evaluated from the I_D/I_G ratio using the four-peak model,[21] follows the order TL9 > YEC > TL9/Cu-40% > YEC/Cu-40% (Table S2). Specifically, TL9 (3.42) exhibits higher disorder and edge-plane exposure than YEC (2.94). After Cu_2O incorporation, I_D/I_G increases to 3.83 and 3.06 for TL9/Cu-40% and YEC/Cu-40%, respectively, indicating that Cu_2O disrupts the sp^2 network and introduces additional defects.[22] On the other hands, N-doped defect sites—particularly pyridinic and pyrrolic N—are known to act as preferential anchoring centers for Cu-based species. During Cu_2O deposition, these pre-existing defects may be selectively occupied rather than newly generated. Hence the attachment of Cu_2O nanoparticles at these defect-rich regions perturbs the local π-conjugation and modifies the Raman scattering cross-section of neighboring bonds.[23] Because Raman spectroscopy provides a spatially averaged measure of disorder, the preferential consumption and electronic modification of defect sites can manifest as a higher apparent I_D/I_G ratio. Therefore, the observed increase likely reflects a combination of (i) perturbation of the sp^2 lattice at metal–support interfaces and (ii) selective deposition of Cu_2O onto intrinsic defect sites. The smaller increase of I_D/I_G ratio in YEC/Cu-40% suggests weaker Cu_2O anchoring on YEC compared to TL9.

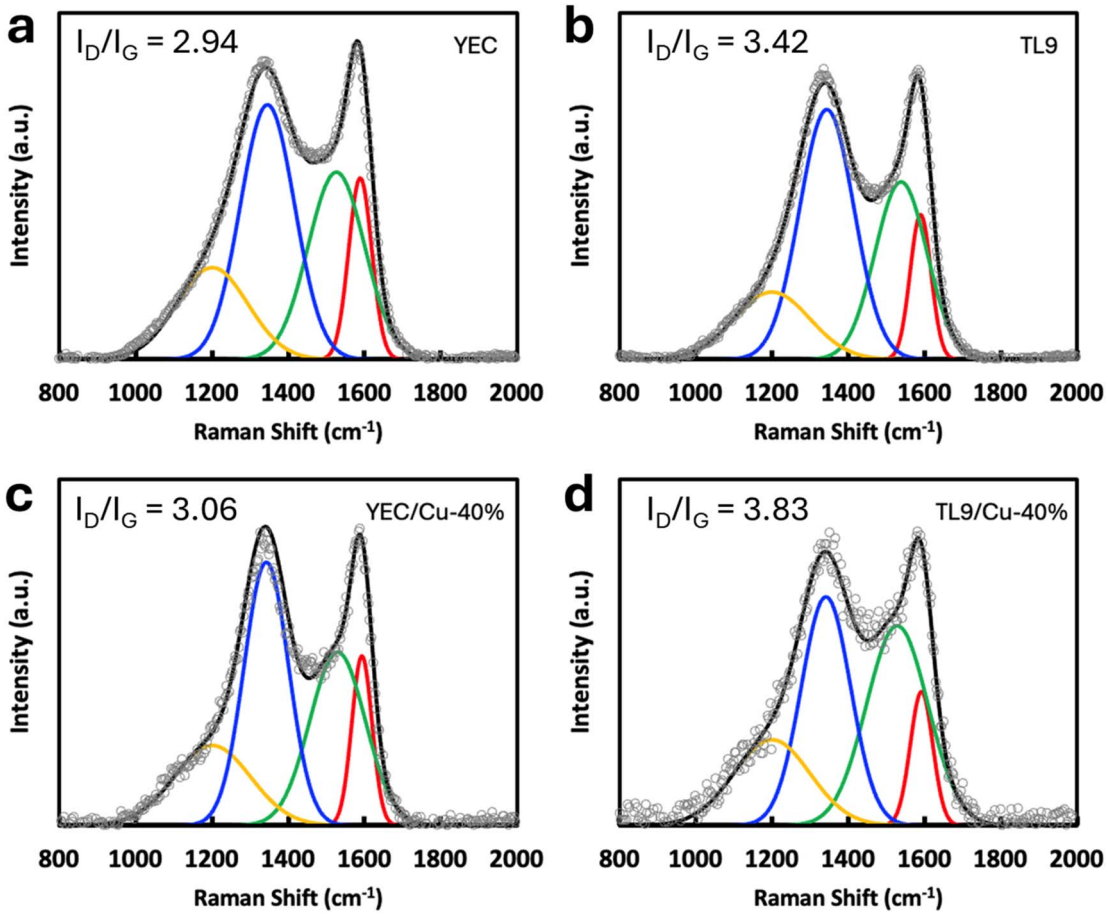

Fig. 2 Raman spectra of (a) YEC, (b) TL9 (c) YEC/Cu-40%, and (d) TL9/Cu-40%. Note that the circle and solid lines represent the raw data and curve fitting after peak deconvolution, respectively. The peak intensity ratio, I_D/I_G, is also shown in each figure.

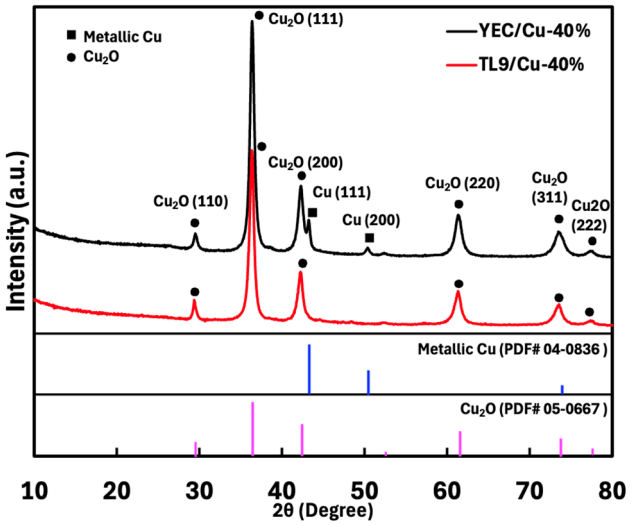

Fig. 3 XRD patterns corresponded to YEC/Cu-40% and TL9/Cu-40% together with the references, metallic Cu and Cu_2O.

Thermogravimetric analysis (TGA, Fig. S2) supports the Raman findings. TL9 exhibits an earlier onset of decomposition—approximately 50 °C lower than YEC—reflecting its more defect-rich and less thermally stable framework.[24] Although such defects decrease structural stability, they are often catalytically beneficial.[25] The residual weight (~20%) of TL9 likely arises from inherent mineral components (K, Si, Ca, Mg, P, Na) in tea-leaf-derived carbon.[26,27] These residues are not catalytically active for CO_2 reduction but can marginally lower the electrical conductivity of the carbon matrix.[28]

X-ray diffraction (XRD) analysis was conducted to determine the crystalline phases of copper species in the composites (Fig. 3). The diffraction peaks of YEC/Cu-40% at 36.4°, 42.3°, and 61.4° correspond to the (111), (200), and (220) planes of cubic Cu_2O (PDF# 05-0667). Additional peaks at 43.3° and 50.4° correspond to metallic Cu (PDF# 04-0836), indicating partial reduction of Cu^+ to Cu^0 during synthesis. Such reduction is typically observed when the Cu precursor lacks sufficient anchoring functionalities.[29] In contrast, TL9/Cu-40% displays

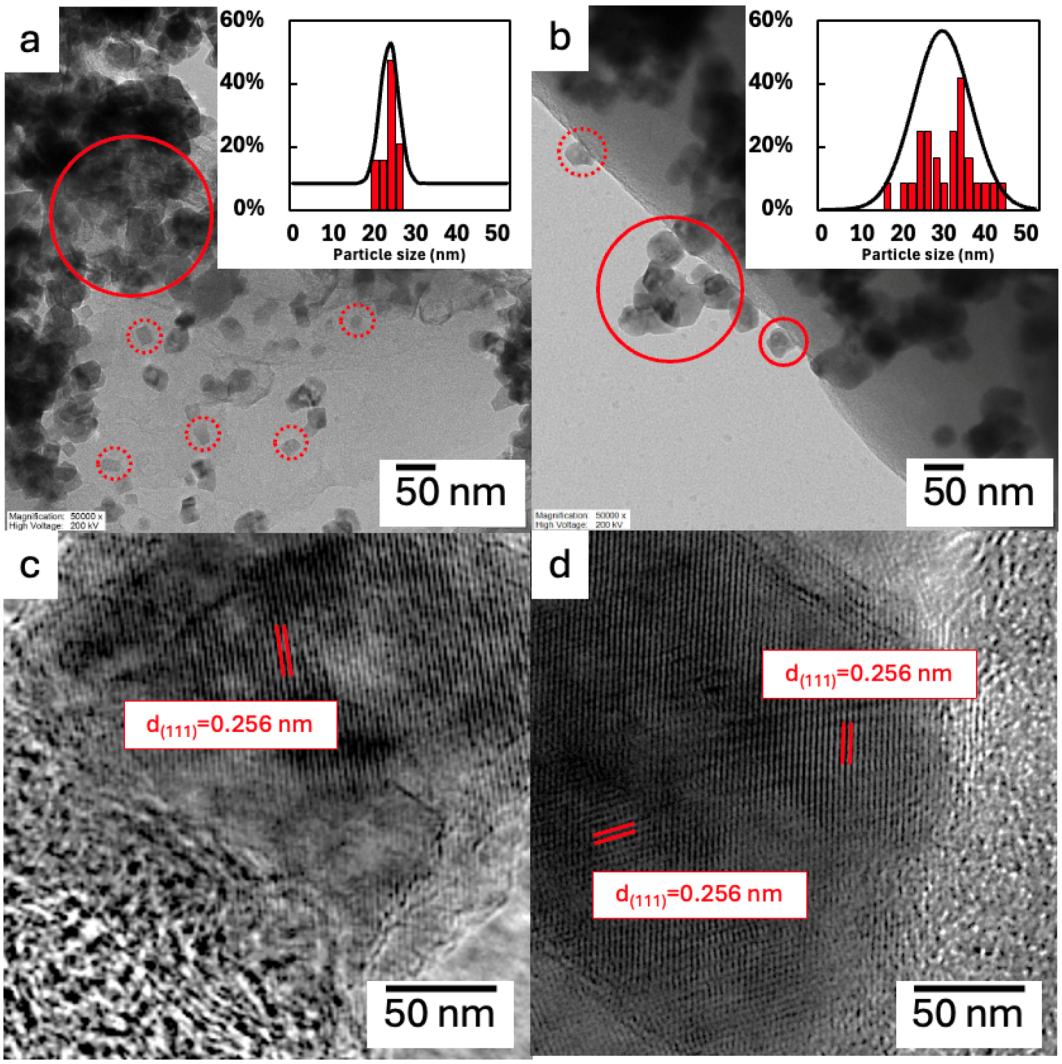

Fig. 4 TEM images of (a) TL9/Cu-40% and (b) YEC/Cu-40% composites. The inset shows particle size distribution of each sample. High-resolution TEM images (c) and (d) highlight lattice fringes corresponding to the (111) plane of Cu_2O (d = 0.256 nm) in both samples.

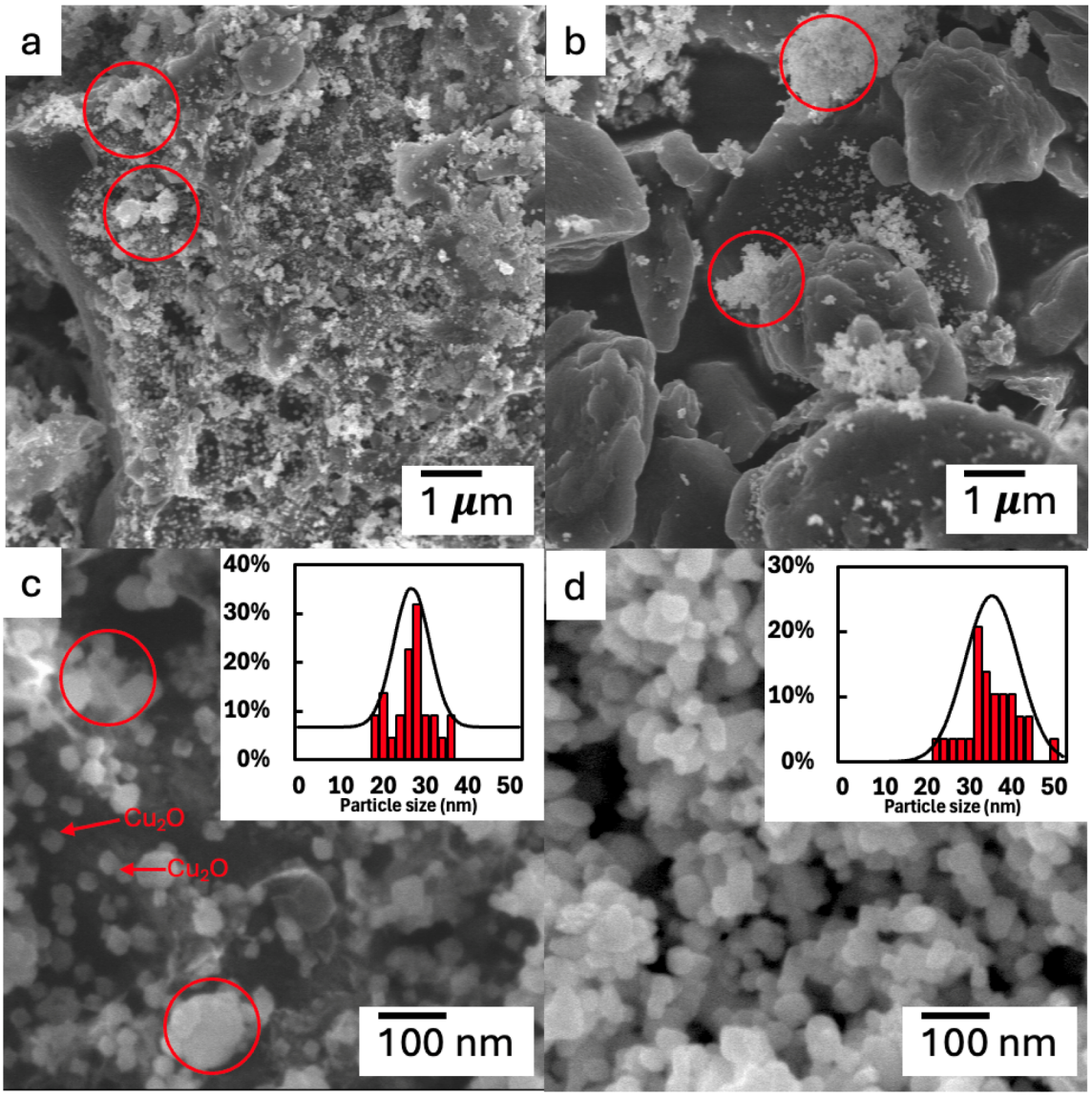

Fig. 5 SEM images of (a) TL9/Cu-40% and (b) YEC/Cu-40% composites along with their high-resolution images (c) and (d). The inset shows particle size distribution of each sample.

only Cu_2O reflections, with no detectable Cu^0 peaks, suggesting that nitrogen functionalities in TL9 stabilize Cu^+ species.[30] The stabilization effect persists across all Cu_2O loadings (10–50%), as confirmed by XRD (Fig. S3).

Based on the Scherrer equation, the average Cu_2O crystallite size was ~16 nm for both TL9/Cu-40% and YEC/Cu-40%. However, transmission electron microscopy (TEM) reveals distinct nanoparticle morphologies (Fig. 4). In YEC/Cu-40%, Cu_2O nanoparticles are agglomerated into polycrystalline structures (~30 nm; Fig. 4b). Conversely, TL9/Cu-40% shows uniformly dispersed Cu_2O nanoparticles with an average diameter of ~20 nm (Fig. 4a). The evolution of Cu_2O dispersion with increasing loading is shown in Fig. S4: at low loadings (10–20%), partial coalescence is observed; at 30%, secondary nucleation leads to uniform nanoparticle formation; and above 40%, agglomeration again dominates.[31,32] High-resolution TEM (Fig. 4c and d) confirms lattice fringes with *d*-spacing of 0.256 nm, consistent with the (111) plane of Cu_2O, with TL9/Cu-40% displaying single-crystal domains while YEC/Cu-40% forms multi-grained polycrystals.

Scanning electron microscopy (SEM, Fig. 5) further supports the TEM results. TL9/Cu-40% exhibits homogeneously distributed Cu_2O nanoparticles across the carbon surface, with few large aggregates (Fig. 5a), whereas YEC/Cu-40% displays large Cu_2O clusters localized in interparticle voids (Fig. 5b). Higher-magnification images reveal average particle sizes of ~27 nm for TL9/Cu-40% and ~35 nm for YEC/Cu-40% (Fig. 5c and d). Although SEM values are slightly larger due to imaging conditions, both analyses confirm superior dispersion and smaller particle size on TL9. The defect-rich surface of TL9 provides abundant anchoring sites, facilitating uniform nucleation and suppressing Cu_2O agglomeration.

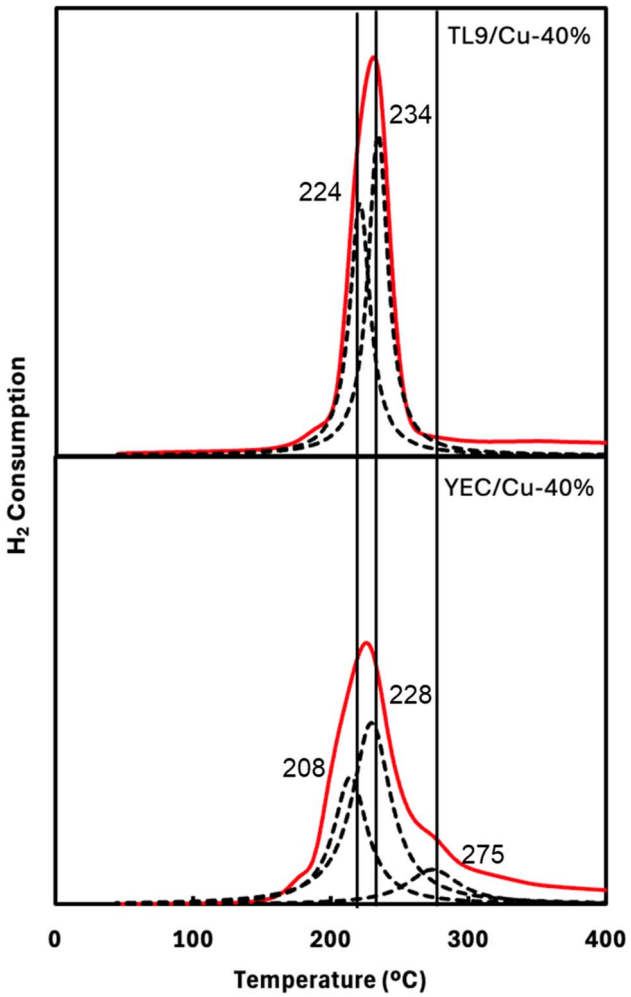

Fig. 6 H_2-TPR profiles corresponded to TL9/Cu-40% and YEC/Cu-40%.

The evolution of Cu_2O morphology with increasing loading on TL9 is illustrated in Fig. S5. At 10%, Cu_2O nanoparticles are well dispersed, nucleating preferentially at defect sites (Fig. S5a). As the loading increases to 20%, these sites become saturated, leading to partial coalescence (Fig. S5b). At 30%, a bimodal microstructure appears, combining agglomerated and newly nucleated nanoparticles (Fig. S5c). At 40%, both coarsened clusters and secondary dispersion coexist (Fig. S5d), whereas at 50% loading, agglomeration becomes dominant (Fig. S5e). This loading-dependent morphological evolution is consistent with nucleation–coalescence dynamics commonly observed in heterogeneous catalytic systems.[31,32]

3.2 Reducibility and surface functionality

The H_2-TPR profiles of the composites exhibit three main peaks at low, moderate, and high temperatures (Fig. 6), corresponding to the stepwise reduction of Cu_2O to metallic Cu. These peaks are associated with the reduction of highly dispersed nanoparticles, loosely bound nanoparticles, and agglomerated Cu_2O particles, respectively.[16,33] For YEC/Cu-40%, the first reduction peak appears at 208 °C. In contrast, TL9/Cu-40% displays two sharp reduction peaks at 221 °C and 234 °C, which can be ascribed to uniformly distributed reducible Cu species of various particle sizes, consistent with the SEM and TEM observations. The upward shift of the first peak for TL9/Cu-40% signifies stronger metal–support interactions.[34] Moreover, YEC/Cu-40% exhibits an additional high-temperature peak at 275 °C, arising from the reduction of highly agglomerated Cu_2O nanoparticles, as evident in the SEM images. The broader and lower-temperature second peak at 228 °C for YEC/Cu-40% further suggests weaker Cu_2O–support interactions compared with TL9/Cu-40%. Together, the H_2-TPR profiles corroborate the microscopic evidence that TL9 effectively promotes uniform Cu_2O dispersion with stronger interfacial bonding.

The reduction behavior of the TL9/Cu series (10–50%) shows a clear loading-dependent trend (Fig. S6). At 10% loading (Fig. S6a), two reduction peaks are observed at 231 °C and 280 °C. The lower-temperature peak reflects strong interactions between Cu_2O and defect sites on TL9,[34] while the higher-temperature peak likely arises from a small fraction of larger nanoparticles.[35,36] As the loading increases to 20% (Fig. S6b), both peaks intensify, indicating a greater number of reducible species. The reduction at 240 °C corresponds to loosely bound Cu_2O clusters, in agreement with TEM (Fig. S4b) and SEM (Fig. S5b) results showing partial coalescence.[32] At 30–40% loadings (Fig. S6c and d), sharper and more intense reduction peaks appear, reflecting the secondary nucleation of Cu_2O nanoparticles and the predominance of uniformly dispersed species. The strong reduction signal at 224 °C for TL9/Cu-40% indicates a higher fraction of these well-dispersed particles relative to TL9/Cu-30%. Partial coalescence remains evident, as seen from the secondary peaks at 237 °C (TL9/Cu-30%) and 234 °C (TL9/Cu-40%). This behavior is consistent with previous reports for supported copper catalysts, where intermediate metal loadings favor homogeneous dispersion and narrow distributions of reducible sites.[16] At 50% loading (Fig. S6e), a new peak emerges at 248 °C, indicating the formation of larger, weakly bound aggregates similar to those in YEC/Cu-40% (Fig. S6f). Overall, the 30–40% loading range yields the most uniform and reducible Cu species, whereas excessive loading promotes heterogeneity and particle agglomeration.

The XPS survey spectrum of TL9 (Fig. S7a) confirms the presence of C, N, and O as the main surface elements, with nitrogen comprising 0.43 at%. Upon Cu_2O deposition, distinct Cu 2p signals appear in TL9/Cu-40% (Fig. S7b), confirming successful Cu incorporation. The N 1s spectrum of TL9 (Fig. 7a) exhibits three main peaks at 398.0, 400.0, and 401.0 eV, attributed to pyridinic-, pyrrolic-, and graphitic-N, respectively.[37–40] After Cu_2O loading, a new peak emerges at 396.0 eV, concurrent with a marked decrease in pyrrolic-N intensity (Fig. 7b). The new feature is assigned to nitridic-like Cu–N_x species,[41–44] formed *via* coordination of Cu with deprotonated pyrrolic-N.[45] This coordination facilitates electron donation from N to Cu, stabilizing Cu^+ sites and preventing over-reduction to Cu^0. The resulting Cu–N_x bonding rationalizes the preservation of catalytically active Cu^+/Cu^0 species during CO_2RR.[45,46]

The C 1s spectra (Fig. S8) display typical peaks corresponding to C–C (284.8 eV), C–O (286.0 eV), C=O (288.0 eV), and

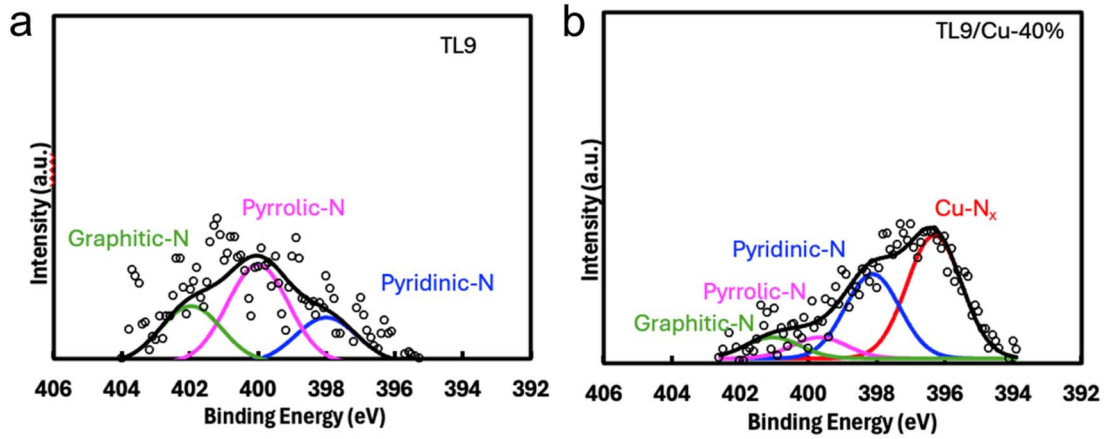

Fig. 7 N 1s spectrum of (a) TL9 and (b) TL9/Cu-40%.

O–C═O (289.6 eV). The O 1s spectra (Fig. S9) reveal components at 531.0 eV (O–C═O), 532.0 eV (C═O), 533.4 eV (C–O), and 535.0 eV (–OH).[47–49] A new feature at 530.5 eV appears in the composites, corresponding to Cu–O bonds in Cu_2O/CuO species, further confirming the presence of Cu_2O.

High-resolution Cu 2p spectra (Fig. 8a) show signals at ~932–933 eV (Cu^+/Cu^0) and ~934–935 eV (Cu^{2+}), with shake-up satellites at 940–945 eV. Because Cu 2p cannot unambiguously distinguish Cu^0 from Cu^+,[13] Cu LMM Auger analysis was performed (Fig. 8b).[50] The Auger spectra reveal that TL9/Cu-40% consists mainly of Cu^+ (~70%), with minor fractions of Cu^0 (~14%) and Cu^{2+} (~16%). By contrast, YEC/Cu-40% contains a larger proportion of Cu^0 (~34%) alongside Cu^+ (~52%) and Cu^{2+} (~14%), as summarized in Table S3. These findings agree well with the XRD results, where metallic Cu reflections appear only in the YEC/Cu composite. Overall, the XPS and TPR analyses confirm that the nitrogen functionalities in TL9 effectively stabilize Cu^+ species, suppressing their reduction to Cu^0 during synthesis.[29] To clarify the origin of Cu–N_x coordination despite the low overall nitrogen content, the evolution of Cu–N_x species

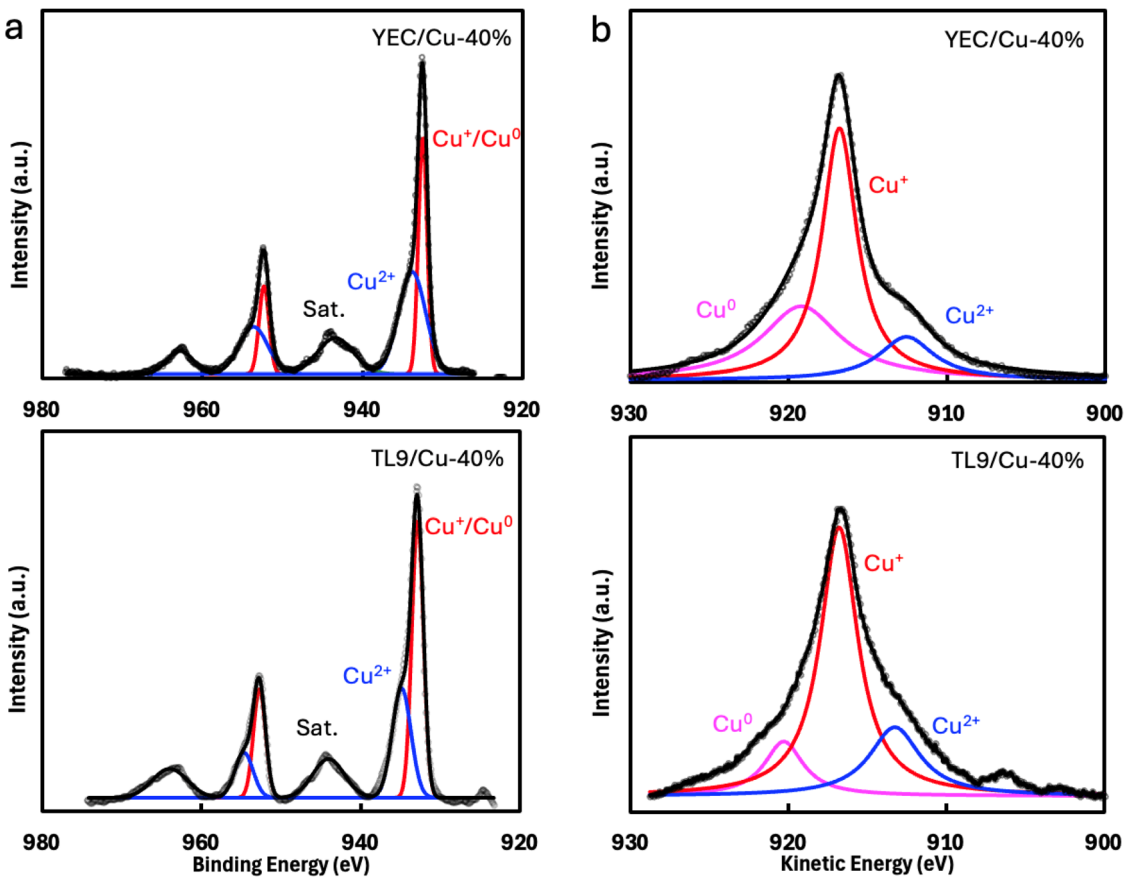

Fig. 8 Cu 2p (left) and Cu LMM (right) spectra of (a) YEC/Cu-40% and (b) TL9/Cu-40%.

with increasing Cu loading was quantified by XPS and is summarized in Fig. S10 and Table S4. Notably, the relationship between Cu at% and Cu–N_x content reveals a distinct saturation trend. The Cu–N_x concentration increases in proportion to Cu loading up to approximately 4.4 at% Cu (corresponding to a nominal loading of 40 wt%), beyond which it reaches a plateau despite further increases in total Cu content. This behavior indicates that nitrogen defect sites offer a finite yet sufficient number of strong anchoring sites that become fully occupied at intermediate Cu loadings. Additional Cu introduced beyond this threshold is therefore deposited predominantly as non-coordinated Cu_2O. These results highlight that effective stabilization of Cu does not require a stoichiometric N–Cu ratio; rather, a small fraction of strategically located nitrogen defects can anchor a large Cu population through localized Cu–N_x coordination.

In summary, the structural, reducibility, and surface analyses collectively demonstrate that TL9 supports the uniform dispersion of Cu_2O nanoparticles strongly anchored at nitrogen defect sites, whereas YEC promotes larger aggregates with weaker metal–support interactions. The stabilization of Cu^+ species in TL9—corroborated by XPS, Cu LMM, and H_2-TPR results—underscores the critical role of nitrogen functionalities in maintaining active Cu^+/Cu^0 interfaces essential for efficient CO_2 reduction catalysis.

3.3 Evaluation of the CO_2RR performances

Electrochemical impedance spectroscopy (EIS) was conducted to elucidate the interfacial kinetics and transport characteristics of the Cu-loaded carbon catalysts. Fig. 9 shows the Nyquist plots and equivalent-circuit fitting for TL9/Cu-40% and YEC/Cu-40%. Both samples exhibit a small semicircle in the high-frequency region, followed by a depressed mid-frequency response and a low-frequency Warburg tail.

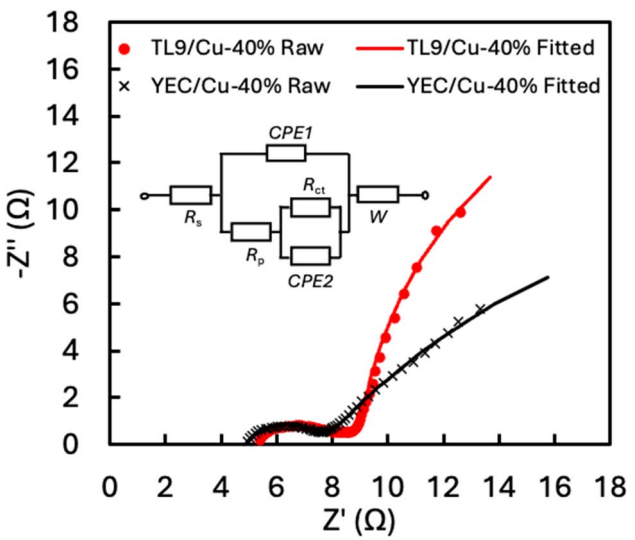

Fig. 9 Nyquist plots for the EIS analysis on the TL9/Cu-40% and the YEC/Cu-40% in 0.5 M $KHCO_3$ solutions after purged with CO_2 for 20 min at open circuit potential (inset: equivalent circuit).

The first high-frequency semicircle is assigned to ion transport within the porous carbon matrix. This interpretation follow the previous reports,[51,52] who demonstrated that porous electrodes inherently display a high-frequency arc originating from pore-channel ion transport. In our system, the high-frequency response is described by a CPE1 with $n \sim 0.55$ for TL9/Cu-40%, which indicates strongly non-ideal capacitive behavior. Such CPE behavior arises when the electrode surface is heterogeneous—typically due to features such as pore networks, surface roughness, and defects—which create a distribution of local double-layer capacitances instead of a single uniform capacitor.[53] Therefore, the CPE in this region reflects the defect-rich and highly porous structure of the TL9 carbon support. The corresponding resistance shown in Table S5 (R_p = 3.43 Ω for TL9/Cu-40% and 2.80 Ω for YEC/Cu-40%), hence reflects pore/film resistance.

The mid-frequency region represents the actual faradaic charge-transfer resistance (R_{ct}) associated with the Cu active sites. Although the semicircle is depressed due to constant-phase behavior and partial overlap with diffusion, equivalent-circuit fitting allows reliable extraction of R_{ct}. TL9/Cu-40% shows a significantly lower charge-transfer resistance (R_{ct} = 26 Ω) compared to YEC/Cu-40% (R_{ct} = 40 Ω), indicating more favorable electron-transfer kinetics. The CPE2 exponent for this branch differs markedly between the two catalysts: TL9/Cu-40% exhibits almost ideal capacitive behavior ($n \sim 1.05$), while YEC/Cu-40% shows strong interfacial heterogeneity ($n \sim 0.60$). These features suggest that the Cu–electrolyte interface in TL9 is more uniform, likely due to better Cu dispersion.

At low frequencies, both catalysts display a Warburg diffusion tail, but the magnitude is substantially larger for YEC/Cu-40%, implying more severe mass-transport limitations within its carbon structure. In contrast, the lower diffusion impedance observed for TL9/Cu-40% indicates more efficient CO_2 and ion transport through its more open pore network.

Overall, the EIS analysis demonstrates that TL9/Cu-40% possesses (i) lower charge-transfer resistance, (ii) more ideal double-layer characteristics, and (iii) reduced diffusion impedance compared to YEC/Cu-40%. These features collectively explain the superior CO_2 reduction activity of the TL9-derived catalyst.

The cyclic voltammetry (CV) profiles (Fig. 10a) show that TL9/Cu-40% exhibits a slightly more negative onset potential (−0.8 V *vs.* RHE) than YEC/Cu-40% (−0.6 V *vs.* RHE), suggesting partial suppression of the hydrogen evolution reaction (HER). HER is primarily governed by surface electronic structure and the availability of metallic Cu^0 and uncoordinated sites. YEC/Cu-40%, which contains a higher fraction of metallic Cu and agglomerated nanoparticles, facilitates rapid H* adsorption and therefore exhibits higher HER currents at a given potential. In contrast, TL9/Cu-40% maintains a higher Cu^+/Cu^0 ratio stabilized by Cu–N_x coordination, which kinetically suppresses hydrogen evolution despite a slightly more negative onset potential.[54,55] This is further supported by electrochemical double-layer capacitance (C_{dl}) measurements (Fig. 10b), where TL9/Cu-40% displays a higher capacitance (72.2 mF cm^{-2}) than YEC/Cu-40% (51.9 mF cm^{-2}), indicative of a larger

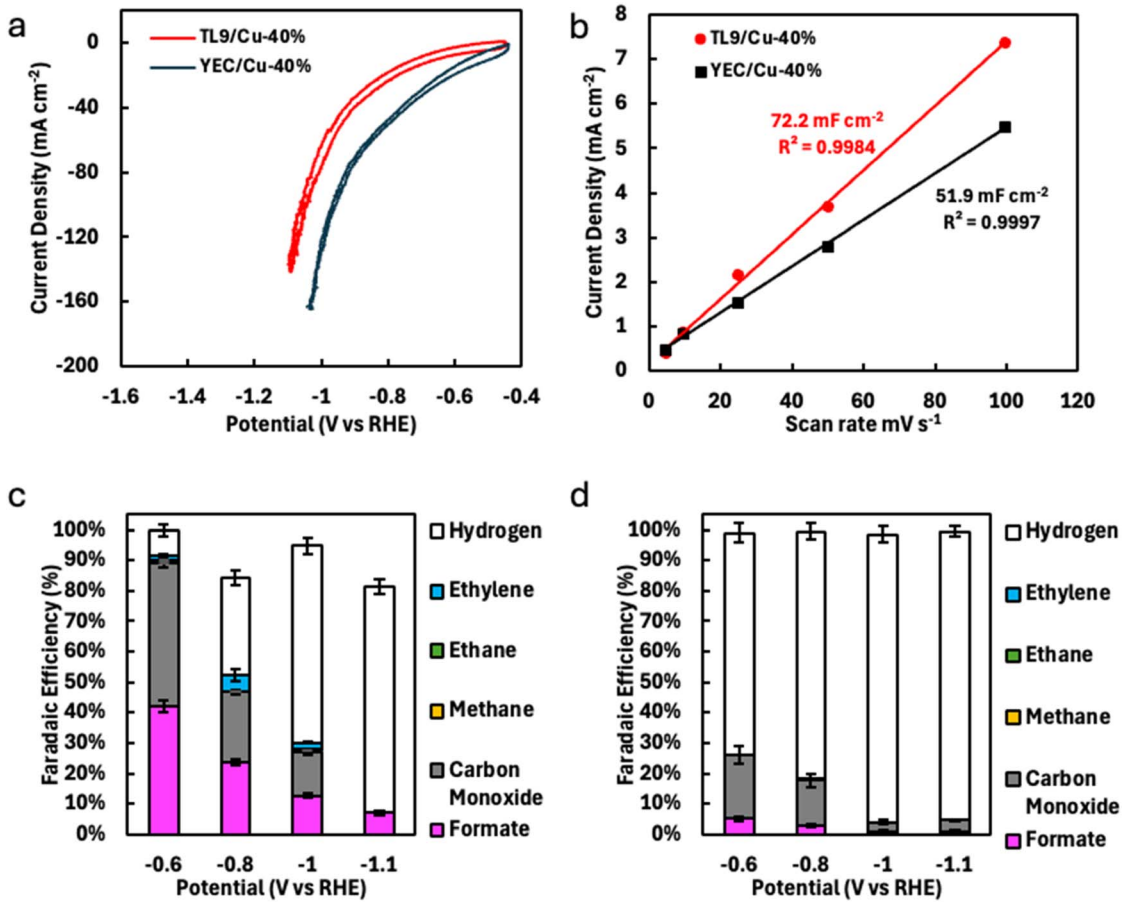

Fig. 10 (a) Cyclic voltammograms and (b) double-layer capacitance (C_{dl}) of TL9/Cu-40% and YEC/Cu-40%. FE of (c) TL9/Cu-40% and (d) YEC/Cu-40% using H-type cell in 0.5 M $KHCO_3$ electrolyte saturated with CO_2 (pH = 7.4).

electrochemically active surface area (ECSA). Despite the slightly delayed onset, TL9/Cu-40% demonstrates markedly superior CO_2RR activity, achieving ~90% FE toward C_1 products at −0.6 V *vs.* RHE, compared with only 28% for YEC/Cu-40% (Fig. 10c and d). Remarkably, even at −0.8 V—where HER typically dominates—the FE of TL9/Cu-40% remains above 50%, underscoring its strong CO_2RR selectivity.

During CO_2 electroreduction, the Cu oxidation state dynamically evolves toward a mixed Cu^+/Cu^0 interface.[30,56] Cu^+ sites stabilize key intermediates such as *COOH (for CO) and *OCHO (for formate), whereas neighboring Cu^0 domains promote electron transfer, product desorption, and C–C coupling toward C_2^+ products.[13,56,57] Unstabilized Cu^+ species tend to reduce to Cu^0, forming so-called oxide-derived Cu (OD-Cu), which mainly produces CO through the *COOH pathway.[12] Nitrogen species may also act as HER sites,[58] thus competing with CO_2RR. XPS analysis confirmed that TL9/Cu-40% retains a larger Cu^+ fraction than YEC/Cu-40%, consistent with the stabilizing effect of N dopants that anchor Cu^+ and suppress its full reduction to metallic Cu. This stabilization preserves a favorable Cu^+/Cu^0 balance during operation, optimizing C_1-product formation.[1] The persistence of Cu^+ at N-anchored sites promotes selective CO and formate generation,[57] whereas the dominance of metallic Cu and exposed N sites in YEC/Cu-40% results in lower CO_2RR selectivity and CO as the major product. These results confirm that the Cu_2O–N-carbon interaction critically governs the reaction pathway by sustaining catalytically active Cu^+/Cu^0 interfaces.[59]

The superior CO_2RR activity of TL9/Cu-40% arises from the uniform dispersion and strong anchoring of Cu_2O nanoparticles at nitrogen defect sites. Homogeneously distributed Cu species offer a higher density of electronically consistent active centers, reflected by the larger C_{dl} (72.2 mF cm^{-2} *vs.* 51.9 mF cm^{-2} for YEC/Cu-40%), and thus a greater ECSA.[60,61] These features facilitate the stabilization of *COOH and *OCHO intermediates and enhance electron transfer while suppressing HER. Consequently, TL9/Cu-40% sustains >50% FE for CO_2RR even at −0.8 V, a potential at which HER typically dominates. In contrast, agglomerated Cu_2O in YEC/Cu-40% lowers the effective ECSA and exposes non-Cu sites that favor hydrogen evolution. These findings underscore that nanoscale dispersion and interfacial uniformity are decisive factors translating directly into CO_2RR activity and selectivity.

CV curves of TL9/Cu composites with varying Cu_2O loadings (10–50%) are presented in Fig. S11a. All samples show similar onset potentials near −0.8 V *vs.* RHE, suggesting that CO_2 activation thermodynamics are relatively unaffected by loading. However, the catalytic current increases markedly from 10 to

40%, reflecting enhanced ECSA (Fig. S11b). At 50%, the current slightly declines, implying that excessive Cu_2O induces nanoparticle agglomeration, which impedes charge transfer and site accessibility.[62] The corresponding FEs (Fig. S11c–f) reveal that at 10% (Fig. S11c), H_2 is the dominant product, with limited CO and formate formation due to the low ECSA and exposure of uncoordinated N sites that favor HER.[58] Increasing the loading to 20% (Fig. S11d) enhances CO production, but formate selectivity remains low because Cu_2O agglomeration reduces the stabilized Cu^+ fraction, favoring the *COOH pathway. At 30% (Fig. S11e), CO_2RR activity improves significantly, producing both CO and formate, attributed to a balanced Cu^+/Cu^0 ratio from more uniform Cu_2O coverage. The highest performance occurs at 40% (Fig. 10c), where optimal Cu^+/Cu^0 balance yields abundant active sites and an FE of ~90% toward CO_2RR products. Further increasing the loading to 50% (Fig. S11f) lowers formate selectivity and increases H_2 (~20%), consistent with agglomeration observed by SEM and H_2-TPR. This aggregation diminishes the stabilized Cu^+ fraction, similar to the 20% sample, leading again to CO-dominated products.

Long-term electrolysis (Fig. 11) further demonstrates the stability advantage of TL9/Cu-40%. All long-term electrolysis performed under identical conditions at an applied potential of −0.6 V *vs.* RHE in CO_2-saturated 0.5 M $KHCO_3$ with a CO_2 flow rate of 20 sccm. The FE for TL9/Cu-40% remains above 60% after 24 h, with current density stabilizing at ~1.5 mA cm^{-2}. This modest decline suggests partial surface restructuring yet retention of a significant fraction of active Cu^+/Cu^0 sites.[63] By contrast, YEC/Cu-40% exhibits rapid deactivation, with FE dropping from ~25% to <15% and current density declining substantially, consistent with weaker Cu–support interactions leading to Cu_2O agglomeration and irreversible reduction to Cu^0. Overall, these observations confirm that nitrogen defect anchoring in TL9 not only enhances CO_2RR activity and selectivity but also mitigates degradation, enabling sustained catalytic performance under prolonged operation.

To further confirm the identity of the liquid-phase product, the post-electrolysis electrolyte was analyzed by ^{1}H NMR and HPLC. As shown in Fig. S13, a distinct resonance at ~8.4 ppm, characteristic of formate, was observed in the ^{1}H NMR spectrum, with no detectable signals from other liquid products. Quantitative HPLC chromatogram of the post-electrolysis electrolyte (Fig. S14), together with the corresponding calibration curve (Fig. S15), further confirms formate as the dominant liquid product.

3.4 Post-CO_2RR surface functionalities

To directly verify the stabilizing effect of TL9 on Cu^+ species, post-CO_2RR Cu LMM Auger XPS analysis was performed and compared with the pristine catalysts, as shown in Fig. S12. The relative fractions of Cu^+, Cu^0, and Cu^{2+} were quantified by peak deconvolution and are summarized in Table S6.

As shown in Fig. S12a, TL9/Cu-40% before CO_2RR consists predominantly of Cu^+ species (~64%), with only a minor contribution from Cu^0 (~14%). After 24 h of CO_2 electroreduction (Fig. S12a, bottom), the Cu LMM spectrum of TL9/Cu-40% shows that a substantial fraction of Cu^+ is retained (~36%), with only a moderate increase in the Cu^0 component. Importantly, the Cu^+ peak position and intensity remain clearly discernible, indicating that Cu^+ is not fully reduced to metallic Cu during prolonged operation.

In contrast, YEC/Cu-40% (Fig. S12b) exhibits a markedly different behavior. Even before CO_2RR, YEC/Cu-40% contains a larger fraction of Cu^0 (~34%), consistent with weaker metal–support interactions. After CO_2RR, the Cu LMM spectrum shows a dominant Cu^0 signal, with Cu^+ becoming a minor component, evidencing extensive reduction of Cu^+ to Cu^0 during electrolysis.

Beyond demonstrating Cu^+ stabilization, post-electrolysis Cu LMM Auger XPS analysis provides direct insight into the degradation mechanism. The observed decline in FE over extended electrolysis can be rationalized by several concurrent degradation processes. First, weakly stabilized Cu^+ sites that are not strongly coordinated to nitrogen defects are preferentially reduced or lost during prolonged operation, whereas Cu^+ species anchored through robust Cu–N_x interactions remain

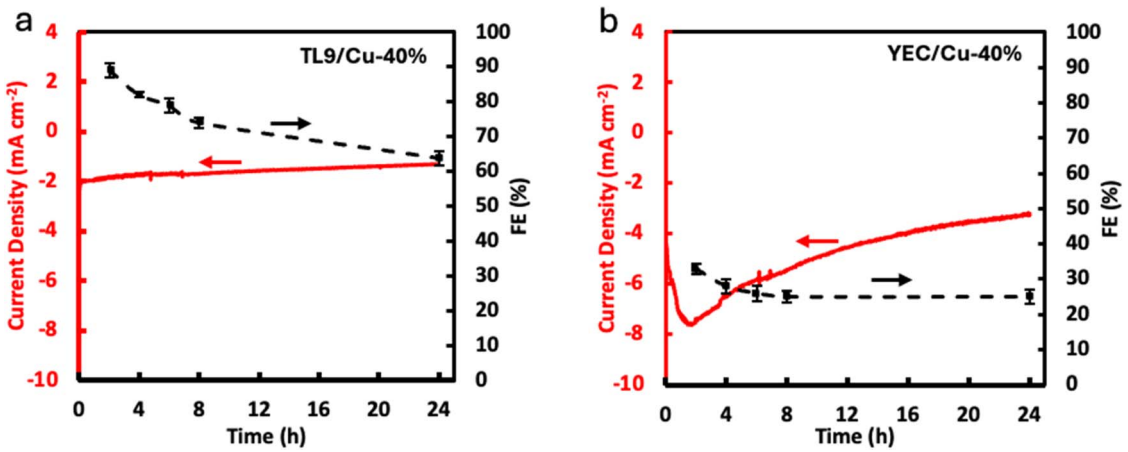

Fig. 11 Stability test of (a) TL9/Cu-40% and (b) YEC/Cu-40% at 0.6 V *vs.* RHE using H-type cell in 0.5 M $KHCO_3$ electrolyte saturated with CO_2 (pH = 7.4) for 24 hours.

catalytically active.[10] Second, sustained cathodic polarization induces electrochemical surface reconstruction, driven by local pH gradients, Cu atom migration, and dynamic restructuring of the catalyst surface.[64,65] Finally, these processes promote the gradual growth of metallic Cu domains, which tend to favor hydrogen evolution and CO formation over the formate pathway.[66] As a result, the relative contribution of C_1 products decreases with time, leading to the observed reduction in overall selectivity despite the persistence of strongly stabilized Cu–N_x active sites.

Therefore, the performance decay reflects bias-induced Cu^+ evolution rather than failure of the Cu^+ stabilization mechanism, and the superior long-term selectivity of TL9/Cu-40% compared to YEC/Cu-40% directly supports the role of nitrogen defects in mitigating electrochemical degradation.

4. Conclusion

In summary, N-doped carbon derived from tea leaves provides a defect-rich scaffold that anchors Cu_2O nanoparticles and stabilizes Cu^+ species through strong Cu–N_x coordination. This interfacial stabilization enables a persistent Cu^+/Cu^0 synergy that drives efficient CO_2 electroreduction to CO and formate while mitigating hydrogen evolution and catalyst deactivation. The optimized TL9/Cu–40% catalyst exhibits uniform Cu_2O dispersion, high FE (~90%), and long-term operational stability exceeding 24 h. In contrast, Cu supported on commercial activated carbon suffers from particle agglomeration and loss of Cu^+ activity, underscoring the crucial role of metal–support interactions. By integrating surface defect engineering with sustainable biomass-derived carbons, this work redefines pathways toward scalable, selective, and stable CO_2 conversion. The demonstrated control over oxidation-state dynamics and dual product selectivity positions TL9/Cu as a model bifunctional system for the advanced electrocatalysts that merge material design with electrochemical functionality to unlock the next generation of CO_2-to-chemicals technologies.

Conflicts of interest

There are no conflicts to declare.

Data availability

The data supporting this article have been included as part of the supplementary information (SI): Tables S1–S6, additional N_2 adsorption-desorption isotherms, TGA plots, XRD patterns of the composites with various Cu_2O loading on TL9, additional TEM and SEM images, H_2-TPR profiles, XPS survey spectrum, C 1s spectra, and O 1s spectra, correlation between Cu atomic percentage and Cu–N□, additional catalytic performances, Cu LMM spectra before and after CO_2RR electrolysis, ^{1}H NMR and HPLC data. See DOI: https://doi.org/10.1039/d5ra08966b.

Acknowledgements

This research was supported by Thailand Science Research and Innovation (TSRI) Fundamental Fund, fiscal year 2025. P. A. acknowledges the graduate scholarship under the SIIT-JAIST Dual Doctoral Degree Program. P. S. acknowledges the support from Thammasat Post Doctoral Fellowship (Contract No. TUPD 4/2567).

References

1 R.-Z. Xiong, H.-M. Xu, H.-R. Zhu, Z.-J. Zhang and G.-R. Li, Recent progress in Cu-based electrocatalysts for CO_2 reduction, *Chem. Eng. J.*, 2025, **505**, 159210.
2 H. Xie, T. Wang, J. Liang, Q. Li and S. Sun, Cu-based nanocatalysts for electrochemical reduction of CO_2, *Nano Today*, 2018, **21**, 41–54.
3 T.-C. Chou, C.-C. Chang, H.-L. Yu, W.-Y. Yu, C.-L. Dong, J.-J. Velasco-Vélez, *et al.*, Controlling the Oxidation State of the Cu Electrode and Reaction Intermediates for Electrochemical CO_2 Reduction to Ethylene, *J. Am. Chem. Soc.*, 2020, **142**(6), 2857–2867.
4 H. Tabassum, X. Yang, R. Zou and G. Wu, Surface engineering of Cu catalysts for electrochemical reduction of CO_2 to value-added multi-carbon products, *Chem Catal.*, 2022, **2**(7), 1561–1593.
5 E. Schuler, M. Morana, P. A. Ermolich, K. Lüschen, A. J. Greer, S. F. R. Taylor, *et al.*, Formate as a key intermediate in CO_2 utilization, *Green Chem.*, 2022, **24**(21), 8227–8258.
6 G. Centi, E. A. Quadrelli and S. Perathoner, Catalysis for CO_2 conversion: a key technology for rapid introduction of renewable energy in the value chain of chemical industries, *Energy Environ. Sci.*, 2013, **6**(6), 1711–1731.
7 M. Ronda-Lloret, G. Rothenberg and N. R. Shiju, A Critical Look at Direct Catalytic Hydrogenation of Carbon Dioxide to Olefins, *ChemSusChem*, 2019, **12**(17), 3896–3914.
8 Y. Zhang, G. Jacobs, D. E. Sparks, M. E. Dry and B. H. Davis, CO and CO_2 hydrogenation study on supported cobalt Fischer–Tropsch synthesis catalysts, *Catal. Today*, 2002, **71**(3–4), 411–418.
9 A. Vijayakumar, Y. Zhao, K. Wang, Y. Chao, H. Chen, C. Wang, *et al.*, A Nitrogen-Doped Porous Carbon Supported Copper Catalyst from a Scalable One-Step Method for Efficient Carbon Dioxide Electroreduction, *ChemElectroChem*, 2023, **10**(2), e202200817.
10 D. A. Bulushev, A. L. Chuvilin, V. I. Sobolev, S. G. Stolyarova, Y. V. Shubin, I. P. Asanov, *et al.*, Copper on carbon materials: stabilization by nitrogen doping, *J. Mater. Chem. A*, 2017, **5**(21), 10574–10583.
11 H. Ning, X. Wang, W. Wang, Q. Mao, Z. Yang, Q. Zhao, *et al.*, Cubic Cu_2O on nitrogen-doped carbon shells for electrocatalytic CO_2 reduction to C_2H_4, *Carbon*, 2019, **146**, 218–223.
12 D. Cheng, Z.-J. Zhao, G. Zhang, P. Yang, L. Li, H. Gao, *et al.*, The nature of active sites for carbon dioxide electroreduction

over oxide-derived copper catalysts, *Nat. Commun.*, 2021, **12**(1), 395.

13 K. Yue, Y. Qin, H. Huang, Z. Lv, M. Cai, Y. Su, *et al.*, Stabilized Cu^0-Cu^{1+} dual sites in a cyanamide framework for selective CO_2 electroreduction to ethylene, *Nat. Commun.*, 2024, **15**(1), 7820.

14 D. Li, T. Liu, L. Huang, J. Wu, J. Li, L. Zhen, *et al.*, Selective CO_2-to-formate electrochemical conversion with core–shell structured Cu_2O/Cu@C composites immobilized on nitrogen-doped graphene sheets, *J. Mater. Chem. A*, 2020, **8**(35), 18302–18309.

15 S. S. Desa and K. Nueangnoraj, Enhanced Redox Activity of Anthraquinone on N-Doped Porous Carbon Electrode, *ChemistrySelect*, 2024, **9**(21), e202303953.

16 T. Witoon, N. Kachaban, W. Donphai, P. Kidkhunthod, K. Faungnawakij, M. Chareonpanich, *et al.*, Tuning of catalytic CO_2 hydrogenation by changing composition of CuO–ZnO–ZrO_2 catalysts, *Energy Convers. Manage.*, 2016, **118**, 21–31.

17 X. Zhang, X. Xia, I. Ivanov, X. Huang and B. E. Logan, Enhanced activated carbon cathode performance for microbial fuel cell by blending carbon black, *Environ. Sci. Technol.*, 2014, **48**(3), 2075–2081.

18 M. D. Donohue and G. L. Aranovich, Classification of Gibbs adsorption isotherms, *Adv. Colloid Interface Sci.*, 1998, **76–77**, 137–152.

19 V. Georgakilas, J. A. Perman, J. Tucek and R. Zboril, Broad Family of Carbon Nanoallotropes: Classification, Chemistry, and Applications of Fullerenes, Carbon Dots, Nanotubes, Graphene, Nanodiamonds, and Combined Superstructures, *Chem. Rev.*, 2015, **115**(11), 4744–4822.

20 V. Harnchana, S. Chaiyachad, S. Pimanpang, C. Saiyasombat, P. Srepusharawoot, V. Amornkitbamrung, *et al.*, Hierarchical Fe_3O_4-reduced graphene oxide nanocomposite grown on NaCl crystals for triiodide reduction in dye-sensitized solar cells, *Sci. Rep.*, 2019, **9**(1), 1494.

21 A. Sadezky, H. Muckenhuber, H. Grothe, R. Niessner and U. Pöschl, Raman microspectroscopy of soot and related carbonaceous materials: spectral analysis and structural information, *Carbon*, 2005, **43**(8), 1731–1742.

22 M. A. S. M. Haniff, S. M. Hafiz, K. A. Wahid, Z. Endut, M. I. Syono, N. M. Huang, *et al.*, Nitrogen-doped multiwalled carbon nanotubes decorated with copper(I) oxide nanoparticles with enhanced capacitive properties, *J. Mater. Sci.*, 2017, **52**(11), 6280–6290.

23 M. W. Iqbal, A. K. Singh, M. Z. Iqbal and J. Eom, Raman fingerprint of doping due to metal adsorbates on graphene, *J. Phys.: Condens. Matter*, 2012, **24**(33), 335301.

24 F. Farivar, P. L. Yap, R. U. Karunagaran, D. Losic, F. Farivar, P. Lay Yap, *et al.*, Thermogravimetric Analysis (TGA) of Graphene Materials: Effect of Particle Size of Graphene, Graphene Oxide and Graphite on Thermal Parameters, *C*, 2021, **7**(2), 41.

25 M. Suominen and T. Kallio, What We Currently Know about Carbon-Supported Metal and Metal Oxide Nanomaterials in Electrochemical CO_2 Reduction, *ChemElectroChem*, 2021, **8**(13), 2397–2406.

26 S. V. Vassilev, D. Baxter, L. K. Andersen and C. G. Vassileva, An overview of the composition and application of biomass ash. Part 1. Phase–mineral and chemical composition and classification, *Fuel*, 2013, **105**, 40–76.

27 J. Zhai, I. T. Burke, W. M. Mayes and D. I. Stewart, New insights into biomass combustion ash categorisation: a phylogenetic analysis, *Fuel*, 2021, **287**, 119469.

28 X. Zhu, Y. Zeng, X. Zhao, D. Liu, W. Lei and S. Lu, Biomass-Derived Carbon and Their Composites for Supercapacitor Applications: Sources, Functions, and Mechanisms, *EcoEnergy*, 2025, **3**(3), e70000.

29 L. Vivas, I. Chi-Duran, J. Enríquez, N. Barraza, D. P. Singh, L. Vivas, *et al.*, Ascorbic acid based controlled growth of various Cu and Cu_2O nanostructures, *Mater. Res. Express*, 2019, **6**(6), 065033.

30 Y. Shen, L. Qian, Q. Xu, S. Wang, Y. Chen, H. Lu, *et al.*, N-doped Cu_2O with the tunable Cu^0 and Cu^+ sites for selective CO_2 electrochemical reduction to ethylene, *J. Environ. Sci.*, 2025, **150**, 246–253.

31 B. Ahn, L. Bosetti and M. Mazzotti, Secondary Nucleation by Interparticle Energies. II. Kinetics, *Cryst. Growth Des.*, 2021, **22**(1), 74–86.

32 N. T. K. Thanh, N. Maclean and S. Mahiddine, Mechanisms of Nucleation and Growth of Nanoparticles in Solution, *Chem. Rev.*, 2014, **114**(15), 7610–7630.

33 R. Poreddy, C. Engelbrekt and A. Riisager, Copper oxide as efficient catalyst for oxidative dehydrogenation of alcohols with air, *Catal. Sci. Technol.*, 2015, **5**(4), 2467–2477.

34 F. Qi, J. Peng, Z. Liang, J. Guo, J. Liu, T. Fang, *et al.*, Strong metal-support interaction (SMSI) in environmental catalysis: mechanisms, application, regulation strategies, and breakthroughs, *Environ. Sci. Ecotechnology*, 2024, **22**, 100443.

35 H. Silva, C. Mateos-Pedrero, P. Ribeirinha, M. Boaventura, A. Mendes, H. Silva, *et al.*, Low-temperature methanol steam reforming kinetics over a novel CuZrDyAl catalyst, *React. Kinet., Mech. Catal.*, 2015, **115**(1), 321–339.

36 Z. Zhang, H. Che, J. Gao, Y. Wang, X. She, J. Sun, *et al.*, Shape-controlled synthesis of Cu_2O microparticles and their catalytic performances in the Rochow reaction, *Catal. Sci. Technol.*, 2012, **2**(6), 1207–1212.

37 Y.-H. Lee, Y.-F. Lee, K.-H. Chang and C.-C. Hu, Synthesis of N-doped carbon nanosheets from collagen for electrochemical energy storage/conversion systems, *Electrochem. Commun.*, 2011, **13**(1), 50–53.

38 M. Vujković, N. Gavrilov, I. Pašti, J. Krstić, J. Travas-Sejdic, G. Ćirić-Marjanović, *et al.*, Superior capacitive and electrocatalytic properties of carbonized nanostructured polyaniline upon a low-temperature hydrothermal treatment, *Carbon*, 2013, **64**, 472–486.

39 D. X. Oh, S. Shin, C. Lim and D. S. Hwang, Dopamine-Mediated Sclerotization of Regenerated Chitin in Ionic Liquid, *Materials*, 2013, **6**(9), 3826–3839.

40 H. Jiang, L. Liu, K. Zhao, Z. Liu, X. Zhang and S. Hu, Effect of pyridinic- and pyrrolic-nitrogen on electrochemical

performance of Pd for formic acid electrooxidation, *Electrochim. Acta*, 2020, **337**, 135758.

41 G. Greczynski, D. Primetzhofer, J. Lu and L. Hultman, Core-level spectra and binding energies of transition metal nitrides by non-destructive X-ray photoelectron spectroscopy through capping layers, *Appl. Surf. Sci.*, 2017, **396**, 347–358.

42 Y.-M. Chang, J. Leu, B.-H. Lin, Y.-L. Wang and Y.-L. Cheng, Comparison of H_2 and NH_3 Treatments for Copper Interconnects, *Adv. Mater. Sci. Eng.*, 2013, **2013**(1), 825195.

43 L. Zhu, X. Cao, J. Xiao, S. Ma and S. Ta, Structure and photocatalytic properties of TiO_2/Cu_3N composite films prepared by magnetron sputtering, *Mater. Today Commun.*, 2021, **26**, 101739.

44 H. Perez, V. Jorda, P. Bonville, J. Vigneron, M. Frégnaux, A. Etcheberry, *et al.*, Synthesis and Characterization of Carbon/Nitrogen/Iron Based Nanoparticles by Laser Pyrolysis as Non-Noble Metal Electrocatalysts for Oxygen Reduction, *C*, 2018, **4**(3), 43.

45 D. Divya, M. Nandhagopal and S. Thennarasu, Deprotonation of the –NH proton from a pyrrole moiety enables concentration-dependent colorimetric and fluorescence quenching of silver(I) ions, *New J. Chem.*, 2025, **49**(10), 3918–3929.

46 Q. Lu, V. McKee and J. Nelson, Redox-linked pyrrole NH deprotonation in a dicopper azacryptate system, *J. Chem. Soc. Chem. Commun.*, 1994, (5), 649–651.

47 D. Hulicova-Jurcakova, M. Seredych, G. Q. Lu and T. J. Bandosz, Combined Effect of Nitrogen- and Oxygen-Containing Functional Groups of Microporous Activated Carbon on its Electrochemical Performance in Supercapacitors, *Adv. Funct. Mater.*, 2009, **19**(3), 438–447.

48 M. F. R. Pereira, S. F. Soares, J. J. M. Órfão and J. L. Figueiredo, Adsorption of dyes on activated carbons: influence of surface chemical groups, *Carbon*, 2003, **41**(4), 811–821.

49 R. Xie, Y. Jin, Y. Chen and W. Jiang, The importance of surface functional groups in the adsorption of copper onto walnut shell derived activated carbon, *Water Sci. Technol.*, 2017, **76**(11–12), 3022–3034.

50 J.-Y. Huang, X.-D. Zhang, H. Yang, Q.-W. Liu, W.-W. Yuan, W.-C. Lai, *et al.*, Pulsed Strategy Steers the Structural Evolution of Cu Metal–Organic Framework for CO_2 Reduction to Methane, *Chem.–Eur. J.*, 2025, **31**(35), e202500744.

51 L. Xu, Y. Xiao, Z.-X. Yu, Y. Yang, C. Yan and J.-Q. Huang, Revisiting the Electrochemical Impedance Spectroscopy of Porous Electrodes in Li-ion Batteries by Employing Reference Electrode, *Angew. Chem., Int. Ed.*, 2024, **63**(41), e202406054.

52 L. Shreenivasa, K. Yogesh, S. A. Prashanth, R. Viswanatha and S. Ashoka, Enhancement of cycling stability and capacity of lithium secondary battery by engineering highly porous AlV_3O_9, *J. Mater. Sci.*, 2019, **55**(4), 1648–1658.

53 A. Lasia, Impedance of Porous Electrodes, in *Electrochemical Impedance Spectroscopy and its Applications*, Springer, New York, 2014, pp. 203–250.

54 Y. Zhao, D. Su, W. Dong, X. Xu, X. Zhang and Y. Hu, High crystallinity Sn crystals on Ni foam: an ideal bimetallic catalyst for the electroreduction of carbon dioxide to syngas, *RSC Adv.*, 2020, **10**(64), 39026–39032.

55 C. Guo, S. Liu, Z. Chen, B. Li, L. Chen, C. V. Singh, *et al.*, How does mass transfer influence electrochemical carbon dioxide reduction reaction? A case study of Ni molecular catalyst supported on carbon, *Chem. Commun.*, 2021, **57**(11), 1384–1387.

56 J. Dong, Y. Liu, J. Pei, H. Li, S. Ji, L. Shi, *et al.*, Continuous electroproduction of formate via CO_2 reduction on local symmetry-broken single-atom catalysts, *Nat. Commun.*, 2023, **14**(1), 6849.

57 X. Wang, S. Ding, X. Feng and Y. Zhu, High stability copper clusters anchored on N-doped carbon nanosheets for efficient CO_2 electroreduction to HCOOH, *J. Colloid Interface Sci.*, 2024, **653**, 741–748.

58 G.-f. Long, K. Wan, M.-y. Liu, Z.-x Liang, J.-h. Piao and P. Tsiakaras, Active sites and mechanism on nitrogen-doped carbon catalyst for hydrogen evolution reaction, *J. Catal.*, 2017, **348**, 151–159.

59 T. Sasipatworakarn, D. Pikulrat, K. Homlamai, S. Duangdangchote and M. Sawangphruk, Selective conversion of carbon dioxide to formate using few-layer nitrogen-doped graphene on copper foam with enhanced suppression of the hydrogen evolution reaction, *Sustainable Energy Fuels*, 2024, **8**(14), 3164–3173.

60 C. Jiménez, M. I. Cerrillo, F. Martínez, R. Camarillo and J. Rincón, Effect of carbon support on the catalytic activity of copper-based catalyst in CO_2 electroreduction, *Sep. Purif. Technol.*, 2020, **248**, 117083.

61 O. A. Baturina, Q. Lu, M. A. Padilla, L. Xin, W. Li, A. Serov, *et al.*, CO_2 Electroreduction to Hydrocarbons on Carbon-Supported Cu Nanoparticles, *ACS Catal.*, 2014, **4**(10), 3682–3695.

62 X. Tuaev, X. Tuaev, S. Rudi, S. Rudi, P. Strasser and P. Strasser, The impact of the morphology of the carbon support on the activity and stability of nanoparticle fuel cell catalysts, *Catal. Sci. Technol.*, 2016, **6**(23), 8276–8288.

63 Z. Lian, F. Dattila, N. López, Z. Lian, F. Dattila and N. López, Stability and lifetime of diffusion-trapped oxygen in oxide-derived copper CO_2 reduction electrocatalysts, *Nat. Catal.*, 2024, **7**(4), 401–411.

64 Z. Han, D. Han, Z. Chen, J. Gao, G. Jiang, X. Wang, *et al.*, Steering surface reconstruction of copper with electrolyte additives for CO_2 electroreduction, *Nat. Commun.*, 2022, **13**(1), 3158.

65 Y. Zhong, Z. Sun, B. Y. Xia and Y. Su, Structural Reconstruction of Copper-Based Catalysts in CO_2 Electroreduction Reaction: A Comprehensive Review, *Chem.–Eur. J.*, 2025, **31**(27), e202500770.

66 S. Nitopi, E. Bertheussen, S. B. Scott, X. Liu, A. K. Engstfeld, S. Horch, *et al.*, Progress and Perspectives of Electrochemical CO_2 Reduction on Copper in Aqueous Electrolyte, *Chem. Rev.*, 2019, **119**(12), 7610–7672.